HHS Public Access

Author manuscript

J Struct Biol. Author manuscript; available in PMC 2016 September 01.

Published in final edited form as:

J Struct Biol. 2015 September ; 191(3): 299–305. doi:10.1016/j.jsb.2015.07.009.

Effect of fringe-artifact correction on sub-tomogram averaging from Zernike phase-plate cryo-TEM

Gregory P. Kishchenko[1], **Radostin Danev**[3], **Rebecca Fisher**[1], **Jie He**[1], **Chyongere Hsieh**[1], **Michael Marko**[1], and **Haixin Sui**[1,2,*]

[1]Wadsworth Center, New York State Department of Health, Albany, NY 12201

[2]Department of Biomedical Sciences, School of Public Health, University at Albany, Albany, NY 12201

[3]Max Planck Institute of Biochemistry, Department of Molecular Structural Biology, Am Klopferspitz 18, 82152 Martinsried, Germany

Abstract

Zernike phase-plate (ZPP) imaging greatly increases contrast in cryo-electron microscopy, however fringe artifacts appear in the images. A computational de-fringing method has been proposed, but it has not been widely employed, perhaps because the importance of de-fringing has not been clearly demonstrated. For testing purposes, we employed Zernike phase-plate imaging in a cryo-electron tomographic study of radial-spoke complexes attached to microtubule doublets. We found that the contrast enhancement by ZPP imaging made nonlinear denoising insensitive to the filtering parameters, such that simple low-frequency band-pass filtering made the same improvement in map quality. We employed sub-tomogram averaging, which compensates for the effect of the "missing wedge" and considerably improves map quality. We found that fringes (caused by the abrupt cut-on of the central hole in the phase plate) can lead to incorrect representation of a structure that is well-known from the literature. The expected structure was restored by amplitude scaling, as proposed in the literature. Our results show that de-fringing is an important part of image-processing for cryo-electron tomography of macromolecular complexes with ZPP imaging.

Introduction

Cryo-electron tomography (cryo-ET) is a powerful method for determining the three-dimensional architecture of near-native (vitreously frozen) cells and the structure of their organelles and large protein complexes. However, the requirement for low-dose imaging results in images with low contrast (signal-to-noise ratio), which limits data interpretability (McEwen et al., 2002). Zero-loss energy filtering (Grimm et al., 1998) rejects inelastically

*Correspondence: haixin.sui@health.ny.gov.

The authors declare no competing financial interests.

scattered electrons that would otherwise only contribute to noise in the image, and thus approximately doubles contrast without increasing the electron dose. The recent availability of direct-electron detectors, which have a detection quantum efficiency (DQE) superior to CCD cameras, or even to photographic film, also improves the signal-to-noise ratio, and their rapid frame-rate allows post-processing correction of stage drift and beam-induced motion (Bammes et al., 2012; Battaglia et al., 2009; Downing and Mooney, 2008; Grigorieff, 2013; Kühlbrandt, 2014; Li et al., 2013; McMullan et al., 2009a; McMullan et al., 2009b; Tietz, 2008). In addition to the above, we concern ourselves here with in-focus Zernike phase-plate imaging (Danev and Nagayama, 2001; Shiue et al., 2009; Danev et al., 2009), which increases overall contrast by about two times, with a much greater increase at spatial frequencies that would have near-zero transfer when the EM is set to high underfocus. While there are many types of phase plates (Glaeser, 2013), each with its own advantages and disadvantages, the Zernike type has been used for most of the biological results so far published in both single-particle work (Danev and Nagayama, 2008; Murata et al., 2010; Rochat et al., 2011; Shigematsu et al., 2010) and in electron tomography, sometimes followed by sub-tomogram averaging (Dai et al., 2013; Guerrero-Ferreira and Wright, 2014; Murata et al., 2010).

A Zernike phase plate (ZPP), located in the objective-lens back focal plane, consists of a film with a thickness such that the electrostatic inner potential shifts the phase of electrons scattered by the specimen by $\pi/2$ or 90°, while the unscattered electrons pass through a central hole in the film, without such phase shift. The abrupt edge (“cut-on”) of the central hole is the cause of fringing (“ringing”) artifacts in the image (Danev and Nagayama, 2011; Fukuda et al., 2009).

This effect has been largely eliminated by the recently developed Volta phase plate (Danev et al., 2014), which lacks a central hole, but employs a beam-induced modification of the film in the same location. This central “patch” lacks a sharp cut-on, so the fringing artifact is not apparent in the images. Recently, application of the VPP has produced excellent results (Asano et al., 2015, Fukuda et al., 2015).

The VPP does not require precise pre-centering, since it is simply formed during imaging under the proper conditions. After it is formed, the VPP does not tolerate any shift relative to the unscattered beam. Such shift is eliminated in our latest (unpublished) implementation of tilt-series acquisition using phase plates. Thus, if a conventional ZPP were used, it would only need to be centered at the start of the tilt series. With respect to centering, then, there is only a slight advantage of the VPP over the ZPP.

The VPP is very simple to construct, simply a carbon film placed over the objective aperture, with no need for focused-ion-beam milling of a central hole. The VPP is hardly subject to “ageing” in the electron microscope, and thus is reusable for many weeks. These are the major advantages of the VPP over the ZPP. Both types of phase plate must be heated to above 200°, and both types interpose a thin film in the beam, which results in a minor reduction of contrast due to scattering in the film.

Although the physics behind the VPP is not entirely clear, a phase shift appropriate for practical work is achieved. However, the amount of phase shift of a ZPP can be firmly set by specifying the film thicknesses, which can be chosen according to the particular specimen (which might have significant intrinsic phase shift). Although the cut-on of a ZPP is abrupt, is it accurately known, so that it's effect can be computationally reduced. Also, the ZPP may have better transfer at very low spatial frequency, when operated in a microscope with a long objective-lens focal length. Further comparison and analysis is on-going.

The fringe artifacts caused by the sharp cut-on of a ZPP consist of bright halos around high-contrast objects, and also contrast inversion of large objects (Danev et al., 2009; Edgcombe, 2014). To avoid these complications to data interpretation, the periodicity corresponding to the cut-on frequency of the central hole should be twice the size of the specimen object (Danev et al., 2009). The cut-on periodicity is in the range of 20–80 nm for Zernike phase plates in typical TEMs. This may limit the application of Zernike phase-contrast (ZPC) for imaging certain large, isolated features, although fringing affects mainly only the edges of the extended structures typical of electron tomography. The nature of the fringe artifact has been discussed, and a computational method for correction was proposed (Danev et al., 2010). This method has recently been employed in a study of vitreously frozen bacteria (Guerrero-Ferreira and Wright, 2014), in which slices from tomograms made from "de-fringed" tilt images had good contrast and a more "natural" and less-artifactual appearance.

An important aspect of cryo-electron tomography is the prospect for obtaining structural information at molecular resolution. By means of sub-tomogram averaging of molecular motifs, cryo-electron tomography can facilitate identification of macromolecules by their shape, and reveal their relationship to component proteins of the local cellular architecture. For example, cryo-electron tomography with sub-volume averaging has been used to successfully determine the molecular architectures of a number of ciliar/flagellar protein complexes of eukaryotic or bacterial cells in native state and *in situ* (Bui et al., 2008; Downing et al., 2007; Liu et al., 2008; Nicastro et al., 2006; Sui and Downing, 2006). For such work, the voxel intensity of the molecular motif must reliably represent the actual shape of the molecule. Although ZPC imaging improves contrast, the fringing artifacts in the tilt-series images unevenly influence the voxel intensity in the final structural maps, and it had been unclear if this effect was serious enough to lead to incorrect interpretation of the structure.

To address this concern, we carried out a cryo-electron tomographic study of axonemal radial-spoke complexes attached to microtubule doublets, using ZPC imaging with a cut-on periodicity of about 45 nm. The radial spoke is a multi-protein complex attached to the microtubule doublet in the axoneme of eukaryotic motile cilia or flagella (Curry and Rosenbaum, 1993). Using cryo-electron tomography with conventional defocus phase-contrast (DPC) imaging, the 3D structure of the radial spoke has been determined as a large multi-protein complex with a length of about 43nm (Barber et al., 2012; Pigino et al., 2011) residing perpendicularly on the microtubule doublet, a long protein complex with an elliptical cross-section of 23 × 35 nm.

In this report, tomograms were reconstructed with and without computational de-fringing of the tilt-series micrographs, and comparative structural maps of radial spokes were obtained from sub-tomogram averages. Our results show that ZPC imaging produces improved contrast over DPC imaging. The contrast improvement enhances the visibility of structural features by providing more signal, unlike non-linear denoising methods, which rely on modeling and masking the noise. While sub-tomogram averaging enhances structural details due to an increased signal-to-noise ratio, and also reduces the effect of the missing wedge, the halos and fringes surrounding high-contrast objects in the ZPC results introduce artifacts that can lead to misinterpretation. De-fringing using a filter with a super-Gaussian shape is shown to effectively reduce these artifacts. Our results suggest that de-fringing is an essential step for post-imaging data processing of ZPC images, and maximizes correct interpretability at the level of molecular structure.

2.0 Methods

2.1 Specimen preparation

Flagellar axonemes were isolated from wild-type *Chlamydomonas reinhardtii* following the protocol of Witman (Witman, 1986). In brief, flagella were detached from cell bodies by pH shock and then demembranated with 0.1 - 0.2% Nonidet-P-40 in HMEDS buffer (10 mM HEPES, 5 mM $MgSO_4$, 0.5 mM EGTA, and 4% sucrose, at pH 7.0). Disrupting the isolated axonemes using homogenization followed by high salt washes (0.6 M NaCl in HMEDS buffer) resulted in radial spokes attached to the microtubule doublet (Sui and Downing, 2006).

The concentrated sample was resuspended in sucrose-free HMEDS, and 10-nm colloidal gold particles (Ted Pella, Inc) were added before applying the sample to a glow-discharged holey carbon film on a TEM grid. The grid was plunge-frozen in liquid ethane after brief blotting with filter paper at the edge of the grid. The grids were stored under liquid nitrogen until use.

2.2 Tilt-series imaging

Grids were transferred with a Gatan model 914 cryo-transfer holder into a JEOL JEM-2200FS TEM operated at 200 kV using zero-loss energy filtering with a 20 eV slit width. The TEM was equipped with an objective lens of 5 mm focal length and a heated, piezo-controlled phase-plate holder at the back focal plane. A ZPP with a 500-nm-diameter central hole was used (Danev and Nagayama, 2008), giving a cut-on periodicity of about 45 nm. The phase plate was maintained at 200°C before and during data collection. Low-dose tilt-series images were recorded in-focus (as judged by power spectra of the off-axis images), using a semi-automated method that involved manual tracking of the sample and the phase plate central hole. Single-axis series were recorded having 46 images at a 3-degree tilt interval with a total dose of 65 $e^{-}/Å^2$. Images were recorded with a TVIPS F415MP 4k × 4k on-axis CCD camera (TVIPS, Gauting, Germany) employing 2X binning to yield 2048×2048-pixel images with a pixel size of 1 nm relative to the specimen.

Based on power spectra of the tilt-series images, distortion of the CTF, indicative of charging, was not observed. We took no special precautions with respect to contamination

other than using a fresh phase plate and a phase-plate holder heated to 200°C. Prior to starting the tilt series, we recorded an underfocus image with the phase plate in place, and the CTF followed a pattern consistent with a calculated CTF. We did not observe changes in the phase contrast or the fringes during the tilt series. Thus, we conclude that the fringes were caused by the phase-plate cut-on and not additionally by charging of the phase plate.

2.3 Image processing

De-fringing correction of the tilt-series images followed the method published previously (Danev et al., 2010). In brief, with the functional form 1 + (G −1) exp(−(k/R)^P), a series of super-Gaussian profiles in frequency space were generated with gain (G) of 5, and power coefficient (P) ranging from 4 to 12. The filters, as shown in Fig. 3a for power coefficients of 6, 8 and 10, were shifted along the frequency axis to match the cut-on frequency of the ZPP at 0.023 nm^{-1} (Fig. 3b). The amplitudes of the Fourier transforms of the tilt-series images were then multiplied by the spatial-frequency filters. Application of such super-Gaussian filters increases the amplitude in the low-frequency region by five times while leaving the high-frequency region unchanged. A smooth transition is thus introduced in the region of the cut-on, remediating the abrupt change that gives rise to the fringing artifacts.

The tilt series, with and without de-fringing correction, were aligned using gold fiducial markers, and the reconstruction was calculated by weighted back projection using IMOD (Kremer et al., 1996). The excellent contrast aided manual marking of the coordinates of each radial spoke complex, and cubic subvolumes of 81 pixels on a side were extracted. The subvolumes were normalized and then aligned based on cross-correlation with the functions in the EMAN2 and SPARX libraries (Hohn et al., 2007; Tang et al., 2007). The aligned sub-volumes were averaged using the amplitude-weighting method based on data redundancy in Fourier space (Schmid and Booth, 2008).

Before data interpretation, the averaged 3D density map was filtered to 3 nm with a band-pass filter using SPIDER (Frank et al., 1996). The density maps were rendered and displayed with UCSF Chimera (Goddard et al., 2007; Pettersen et al., 2004).

3.0 Results and discussion

3.1 Enhanced contrast and fringes

Tomographic tilt series were collected from vitreously frozen radial-spoke complexes (attached to microtubule doublets). Fig. 1a shows a zero-tilt micrograph, with several local regions magnified to display details. With ZPC imaging, the unprocessed tilt images revealed good contrast in the radial spokes decorating the microtubule doublets.

A series of concentric fringes are clearly observed surrounding high-contrast objects, such as the contaminating ice particles of various diameters as shown in Fig. 1b and 1c (magnified from regions 1 and 2 respectively in Fig. 1a). For small particles, as shown at the arrows in Fig. 1b, the fringes display bright contrast at the edge of the particles, surrounded by rings of oscillating contrast. For large particles, as shown by the arrow in Fig. 1c, the contrast at the particle center can appear inverted. Fringes of the same sort also surround the microtubule doublets, as shown in Fig. 1d (magnified from Region 3 in Fig. 1a). A bright halo appears

next to the microtubules where the root of the radial spokes connect to the doublets, and a dark fringe occurs near the heads of the radial spokes, thus changing the intensity relationship between them. The fringes appear similar to those described previously (Danev and Nagayama, 2011), and are artifacts introduced by the abrupt cut-on at the edge of the central hole in the ZPP.

3.2 Noise reduction

The signal-to-noise ratio of the ZPC tomogram appears to be higher than that in the DPC cryo-tomogram of microtubule doublets published previously (Sui and Downing, 2006). In cross-sections of the tomogram, radial spokes and the associated microtubule doublets are clearly visible with excellent contrast (Fig. 2a). Nevertheless, significant noise, which hinders interpretability of the density map when displayed by 3D rendering software, is still present. Fig. 2a shows a typical sub-volume of a radial spoke extracted from the ZPC cryo-tomogram. The spokes are arranged parallel to each other in an array, indicating a stable and relatively rigid structural interaction between the radial spokes and the microtubule doublets they are attached to.

Low-pass filtering is commonly used to reduce noise in order to improve interpretability in the maps. More advanced noise reduction methods rely on the use of non-linear algorithms, such as bilateral filtering (Frangakis and Hegerl, 2001; Jiang et al., 2003; Tomasi, 1998). Results from bilateral filtering for denoising DPC cryo-tomograms generally vary greatly depending on the input parameters (Jiang et al., 2003). However for ZPC tomograms, we found the results to be insensitive to input parameters. Fig. 2c shows the sub-volume from Fig. 2a after bilateral filtering, and Fig. 2d shows the same sub-volume filtered using a simple Butterworth low-pass filter at half-Nyquist. As seen by comparison of Figs. 2c and 2d, there is very little difference in the results.

3.3 Sub-volume averaging

Sub-volume averaging is a powerful method used to improve the quality of structural maps and the interpretability of repeating motifs within electron tomograms (Briggs, 2013; Winkler et al., 2009). This overcomes two shortcomings of cryo-electron tomography. (1) The tilt range of the TEM specimen stage, usually limited to a maximum of 60–70 degrees, causes a missing wedge in the Fourier space during reconstruction, which results in a z-axis elongation of the 3-D point-spread function (PSF; Radermacher, 1992). (2) The signal-to-noise ratio of a single instance of a structure in the tomogram is poor, due to the need to keep the total electron dose low. Boxing out, aligning, and averaging repeating motifs addresses both problems, and has led to impressive results (Raddi et al., 2012; Schur et al., 2015; Zhao et al., 2013). The effect of the elongated PSF for particles in different orientations within the tomogram is shown in Figs. 2d and 2e. Since the radial spokes have different orientations with respect to the missing wedge, as shown in Figs. 2f and 2g for example, sub-volume averaging fills in the missing wedge and greatly improves structural interpretation. The result form 98 aligned and averaged radial-spoke sub-volumes is shown in Fig. 5a. Compared to individual subvolumes with different orientations of the missing wedge (e.g Figs 2d, and 2e), the averaged subvolume displays a structural map of much better quality.

Our structural map from ZPC tomography and subvolume averaging with only 98 motifs reveals the same structural features as seen in maps from averaging of about 800 to 2,400 sub-volumes after DPC imaging. In particular, there is excellent correspondence in the radial-spoke head domain, distal form the attached microtubule doublet (Barber et al., 2012;Pigino et al., 2011). However in the stalk region near the attachment to the microtubule doublet, the density is narrower than seen in previous studies. In particular, there is a gap at the stalk root where the radial spoke complex attaches to the microtubule doublet (arrow in Fig. 5a). This structural map would suggest a weak structural connection between the radial spoke and the microtubule doublet. However based on the literature, this gap should not be present in wild-type *Chlamydomonas* (Barber et al, 2012;Pigino et al, 2011). The fact that most of the radial spokes in our maps are in a parallel array (Fig. 2a) implies a rigid, strong interaction between these radial spokes and the microtubule doublets, consistent with previous reports. Analyzing our ZPC tilt-series images, we found that the weak densities of the stalk region and the gap at the base are artifacts due to the ZPC fringes, which modified the relative intensity weighting of different regions in the radial-spoke structural map. As shown in Fig. 1d, a bright halo appears next to the microtubule doublet, which weakens the map density at the root of radial spokes, whereas the dark ring of the oscillating contrast, between the two arrows in Fig 1b or 1d, enhances the density at the head domain. Thus, the ZPC fringing artifact led to misinterpretation at the molecular structural level.

3.4 Artifact correction

As mentioned above, the fringing artifacts are caused by the abrupt edge of the central hole in the phase plate. In the power spectrum of a ZPC image, the edge of the hole is located at the “cut-on” frequency. Below the cut-on frequency, no ZPC contrast is produced, leaving mainly low (amplitude) contrast, while the frequencies just above the cut-on are greatly enhanced by ZPC. The abrupt transition can be ameliorated by physical “apodization” (i.e. beveling), but a properly designed filter has been shown to be effective (Danev et al., 2010). The filter seeks to amplify the spatial frequencies below the cut-on in order to match those above it. Since the effect of the cut-on transition is not perfectly sharp, the use of a super-Gaussian function was suggested to ensure a smooth transition across the cut-on.

We have employed this technique in an attempt to correct the effect of fringing artifacts seen in our initial sub-tomogram-averaged structure. We tested a series of power values for the super-Gaussian function. Fig. 3b shows rotational averages of power spectra of a zero-tilt image from the tomographic tilt series. The thick solid line is from the original micrograph with no correction. The thin solid line, dashed line and dotted lines are from images processed with super-Gaussian power of 6, 8, and 10, respectively. The corresponding super-Gaussian functions are plotted in Fig. 3a. As seen in Fig. 3b, amplitude profiles are smoother after filtering. Use of the super-Gaussian power 8 appears to offer the smoothest transition across the cut-on frequency.

To examine the fringe correction results in real space, the ice contamination particles in Figs.1b (diameter about 25 nm) and 1c (diameter about 54 nm) were rotationally averaged in real space before filtering and after application of the filters at three different power values, as shown in Fig. 4. Before filtering, bright halos surround the small particle (arrows in Fig.

4a), the first of which corresponds to the strong peak of the thick solid line as marked by the upwards arrow in Fig. 4c. The downwards arrow in the same figure indicates a weak peak corresponding to the second ring in Fig. 4a. After use of a filter with a super-Gaussian power of 8, the bright halo was reduced significantly (Fig. 4b and the dashed line in Fig. 4c). Similar fringe rings were present In the case of the large particle, but in addition, contrast in the center of the particle was reversed (Figs. 4d and 4f). Use of the super-Gaussian filter substantially corrected the contrast inversion (Fig. 4e).

After applying the super-Gaussian filter with a power of 8 to the tilt-series images, the reconstruction and sub-volume averaging were repeated, as described above. In the new structural map shown in Figs. 5b (isosurface) and 5c (mesh), the radial-spoke stalk and the microtubule are more filled-out compared to the map before de-fringing (Fig. 5a). The gap in the uncorrected map, as indicated by the red arrow, is substantially corrected in the new map, which is now consistent with the structural maps reported in literature.

4.0 Conclusion

ZPC cryo-electron tomography and sub-tomogram averaging of the radial-spoke complex on microtubule doublets of the *Chlamydomonas* axoneme showed that the contrast enhancement by ZPP imaging made nonlinear denoising insensitive to the filtering parameters, such that simple low-frequency band-pass filtering made the same improvement in map quality. The fringing artifacts associated with ZPC imaging could be substantially reduced by super-Gaussian amplitude correction. The fringing artifacts were shown to interfere with faithful structural interpretation, making such filtering a necessity for quantitative imaging with ZPC.

Acknowledgments

We thank Dr. Kuniaki Nagayama for allowing us to collect data using the phase-plate electron microscope at the Okazaki Institute for Integrative Bioscience, and Dr. Zhong Huang for helpful discussions on python programing for image processing. We are also grateful to Prof. George Witman for gifts of *Chlamydomonas reinhardtii*. This work was supported by NIH grants GM103555 to M.M and GM101026 to H.S.

References

Asano S, Fukuda Y, Beck F, Aufderheide A, Förster F, Danev R, Baumeister W. A molecular census of 26S proteasomes in intact neurons. Science. 2015; 347:439–442. [PubMed: 25613890]

Bammes BE, Rochat RH, Jakana J, Chen DH, Chiu W. Direct electron detection yields cryo-EM reconstructions at resolutions beyond 3/4 Nyquist frequency. J Struct Biol. 2012; 177:589–601. [PubMed: 22285189]

Barber CF, Heuser T, Carbajal-Gonzalez BI, Botchkarev VV Jr, Nicastro D. Three-dimensional structure of the radial spokes reveals heterogeneity and interactions with dyneins in Chlamydomonas flagella. Mol Biol Cell. 2012; 23:111–120. [PubMed: 22072792]

Battaglia M, Contarato D, Denes P, Doering D, Giubilato P, Kim TS, Mattiazzo S, Radmilovic V, Zalusky S. A rad-hard CMOS active pixel sensor for electron microscopy. Nuclear Instruments and Methods in Physics Research Section A: Accelerators, Spectrometers, Detectors and Associated Equipment. 2009; 598:642–649.

Briggs JAG. Structural biology in situ - the potential of subtomogram averaging. Curr Opin Struct Biol. 2013; 23:261–267. [PubMed: 23466038]

Bui KH, Sakakibara H, Movassagh T, Oiwa K, Ishikawa T. Molecular architecture of inner dynein arms in situ in Chlamydomonas reinhardtii flagella. J Cell Biol. 2008; 183:923–932. [PubMed: 19029338]

Cambie R, Downing KH, Typke D, Glaeser RM, Jin J. Design of a microfabricated, two-electrode phase-contrast element suitable for electron microscopy. Ultramicroscopy. 2007; 107:329–339. [PubMed: 17079082]

Curry AM, Rosenbaum JL. Flagellar radial spoke: a model molecular genetic system for studying organelle assembly. Cell Motil Cytoskeleton. 1993; 24:224–232. [PubMed: 8477455]

Dai W, Fu C, Raytcheva D, Flanagan J, Khant HA, Liu X, Rochat RH, Haase-Pettingell C, Piret J, Ludtke SJ, Nagayama K, Schmid MF, King JA, Chiu W. Visualizing virus assembly intermediates inside marine cyanobacteria. Nature. 2013; 502:707–710. [PubMed: 24107993]

Danev R, Nagayama K. Transmission electron microscopy with Zernike phase plate. Ultramicroscopy. 2001; 88:243–252. [PubMed: 11545320]

Danev R, Nagayama K. Single particle analysis based on Zernike phase contrast transmission electron microscopy. J Struct Biol. 2008; 161:211–218. [PubMed: 18082423]

Danev R, Nagayama K. Optimizing the phase shift and the cut-on periodicity of phase plates for TEM. Ultramicroscopy. 2011; 111:1305–1315. [PubMed: 21864771]

Danev R, Glaeser RM, Nagayama K. Practical factors affecting the performance of a thin-film phase plate for transmission electron microscopy. Ultramicroscopy. 2009; 109:312–325. [PubMed: 19157711]

Danev R, Kanamaru S, Marko M, Nagayama K. Zernike phase contrast cryo-electron tomography. J Struct Biol. 2010; 171:174–181. [PubMed: 20350600]

Danev R, Buijsse B, Khoshouei M, Plitzko JM, Baumeister W. Volta potential phase plate for in-focus phase contrast transmission electron microscopy. Proc Natl Acad Sci U S A. 2014; 111:15635–15640. [PubMed: 25331897]

Downing KH, Mooney PE. A charge coupled device camera with electron decelerator for intermediate voltage electron microscopy. Rev Sci Instrum. 2008; 79:043702. [PubMed: 18447528]

Downing KH, Sui H, Auer M. Electron tomography: a 3D view of the subcellular world. Anal Chem. 2007; 79:7949–7957. [PubMed: 18044021]

Edgcombe CJ. Imaging of weak phase objects by a Zernike phase plate. Ultramicroscopy. 2014; 136:154–159. [PubMed: 24184389]

Frangakis AS, Hegerl R. Noise reduction in electron tomographic reconstructions using nonlinear anisotropic diffusion. J Struct Biol. 2001; 135:239–250. [PubMed: 11722164]

Frank J, Radermacher M, Penczek P, Zhu J, Li Y, Ladjadj M, Leith A. SPIDER and WEB: Processing and visualization of images in 3D electron microscopy and related fields. J Struct Biol. 1996; 116:190–199. [PubMed: 8742743]

Fukuda Y, Fukazawa Y, Danev R, Shigemoto R, Nagayama K. Tuning of the Zernike phase-plate for visualization of detailed ultrastructure in complex biological specimens. J Struct Biol. 2009; 168:476–484. [PubMed: 19732832]

Fukuda Y, Laugks U, Lučić V, Baumeister W, Danev R. Electron cryotomography of vitrified cells with a Volta phase plate. J Struct Biol. 2015 pii: S1047-8477(15)00058-1. Epub ahead of print. 10.1016/j.jsb.2015.03.004

Glaeser RM. Invited Review Article: Methods for imaging weak-phase objects in electron microscopy. Rev Sci Instrum. 2013; 84:111101. [PubMed: 24289381]

Goddard TD, Huang CC, Ferrin TE. Visualizing density maps with UCSF Chimera. J Struct Biol. 2007; 157:281–287. [PubMed: 16963278]

Grigorieff N. Direct detection pays off for electron cryo-microscopy. eLife. 2013; 2

Grimm, Typke; Baumeister. Improving image quality by zero-loss energy filtering: quantitative assessment by means of image cross-correlation. Journal of Microscopy. 1998; 190:339–349.

Guerrero-Ferreira RC, Wright ER. Zernike phase contrast cryo-electron tomography of whole bacterial cells. J Struct Biol. 2014; 185:129–133. [PubMed: 24075950]

Hohn M, Tang G, Goodyear G, Baldwin PR, Huang Z, Penczek PA, Yang C, Glaeser RM, Adams PD, Ludtke SJ. SPARX, a new environment for Cryo-EM image processing. J Struct Biol. 2007; 157:47–55. [PubMed: 16931051]

Jiang W, Baker ML, Wu Q, Bajaj C, Chiu W. Applications of a bilateral denoising filter in biological electron microscopy. J Struct Biol. 2003; 144:114–122. [PubMed: 14643214]

Kremer JR, Mastronarde DN, McIntosh JR. Computer visualization of three-dimensional image data using IMOD. J Struct Biol. 1996; 116:71–76. [PubMed: 8742726]

Kühlbrandt W. Cryo-EM enters a new era. eLife. 2014; 3:e03678. [PubMed: 25122623]

Li X, Mooney P, Zheng S, Booth CR, Braunfeld MB, Gubbens S, Agard DA, Cheng Y. Electron counting and beam-induced motion correction enable near-atomic-resolution single-particle cryo-EM. Nat Methods. 2013; 10:584–590. [PubMed: 23644547]

Liu J, Bartesaghi A, Borgnia MJ, Sapiro G, Subramaniam S. Molecular architecture of native HIV-1 gp120 trimers. Nature. 2008; 455:109–113. [PubMed: 18668044]

McEwen BF, Marko M, Hsieh CE, Mannella C. Use of frozen-hydrated axonemes to assess imaging parameters and resolution limits in cryoelectron tomography. J Struct Biol. 2002; 138:47–57. [PubMed: 12160700]

McMullan G, Chen S, Henderson R, Faruqi AR. Detective quantum efficiency of electron area detectors in electron microscopy. Ultramicroscopy. 2009a; 109:1126–1143. [PubMed: 19497671]

McMullan G, Faruqi AR, Henderson R, Guerrini N, Turchetta R, Jacobs A, van Hoften G. Experimental observation of the improvement in MTF from backthinning a CMOS direct electron detector. Ultramicroscopy. 2009b; 109:1144–1147. [PubMed: 19541421]

Murata K, Liu X, Danev R, Jakana J, Schmid MF, King J, Nagayama K, Chiu W. Zernike Phase Contrast Cryo-Electron Microscopy and Tomography for Structure Determination at Nanometer and Subnanometer Resolutions. Structure. 2010; 18:903–912. [PubMed: 20696391]

Nicastro D, Schwartz C, Pierson J, Gaudette R, Porter ME, McIntosh JR. The molecular architecture of axonemes revealed by cryoelectron tomography. Science. 2006; 313:944–948. [PubMed: 16917055]

Pettersen EF, Goddard TD, Huang CC, Couch GS, Greenblatt DM, Meng EC, Ferrin TE. UCSF Chimera--a visualization system for exploratory research and analysis. J Comput Chem. 2004; 25:1605–1612. [PubMed: 15264254]

Pigino G, Bui KH, Maheshwari A, Lupetti P, Diener D, Ishikawa T. Cryoelectron tomography of radial spokes in cilia and flagella. J Cell Biol. 2011; 195:673–687. [PubMed: 22065640]

Raddi G, Morado DR, Yan J, Haake DA, Yang XF, Liu J. Three-dimensional structures of pathogenic and saprophytic Leptospira species revealed by cryo-electron tomography. J Bacteriol. 2012; 194:1299–1306. [PubMed: 22228733]

Radermacher, M. Weighted backprojection methods. In: Frank, J., editor. Electron Tomography: Three-Dimensional Imaging with the Transmission Electron Microscope. Plenum; New York: 1992.

Rochat RH, Liu X, Murata K, Nagayama K, Rixon FJ, Chiu W. Seeing the portal in herpes simplex virus type 1 B capsids. Journal of virology. 2011; 85:1871–1874. [PubMed: 21106752]

Schmid MF, Booth CR. Methods for aligning and for averaging 3D volumes with missing data. J Struct Biol. 2008; 161:243–248. [PubMed: 18299206]

Schur FK, Hagen WJ, Rumlova M, Ruml T, Muller B, Krausslich HG, Briggs JA. Structure of the immature HIV-1 capsid in intact virus particles at 8.8 A resolution. Nature. 2015; 517:505–508. [PubMed: 25363765]

Shigematsu H, Sokabe T, Danev R, Tominaga M, Nagayama K. A 3.5-nm structure of rat TRPV4 cation channel revealed by Zernike phase-contrast cryoelectron microscopy. The Journal of biological chemistry. 2010; 285:11210–11218. [PubMed: 20044482]

Shiue J, Chang CS, Huang SH, Hsu CH, Tsai JS, Chang WH, Wu YM, Lin YC, Kuo PC, Huang YS, Hwu Y, Kai JJ, Tseng FG, Chen FR. Phase TEM for biological imaging utilizing a Boersch electrostatic phase plate: theory and practice. Journal of Electron Microscopy. 2009; 58:137–145. [PubMed: 19289850]

Sui H, Downing KH. Molecular architecture of axonemal microtubule doublets revealed by cryo-electron tomography. Nature. 2006; 442:475–478. [PubMed: 16738547]

Tang G, Peng L, Baldwin PR, Mann DS, Jiang W, Rees I, Ludtke SJ. EMAN2: an extensible image processing suite for electron microscopy. J Struct Biol. 2007; 157:38–46. [PubMed: 16859925]

Tietz H. Design and Characterization of 64 MegaPixel Fiber Optic Coupled CMOS Detector for Transmission Electron Microscopy. Microscopy and Microanalysis. 2008; 14:804–805.

Tomasi, C. In: Manduchi, R., editor. Bilateral Filtering for Gray and Color Images; Proceedings of the 1998 IEEE International Conference on Computer Vision; Bombay, India. 1998. p. 839-839.

Winkler H, Zhu P, Liu J, Ye F, Roux KH, Taylor KA. Tomographic subvolume alignment and subvolume classification applied to myosin V and SIV envelope spikes. J Struct Biol. 2009; 165:64–77. [PubMed: 19032983]

Witman GB. Isolation of Chlamydomonas flagella and flagellar axonemes. Methods Enzymol. 1986; 134:280–290. [PubMed: 3821567]

Zhao X, Zhang K, Boquoi T, Hu B, Motaleb MA, Miller KA, James ME, Charon NW, Manson MD, Norris SJ, Li C, Liu J. Cryoelectron tomography reveals the sequential assembly of bacterial flagella in Borrelia burgdorferi. Proc Natl Acad Sci U S A. 2013; 110:14390–14395. [PubMed: 23940315]

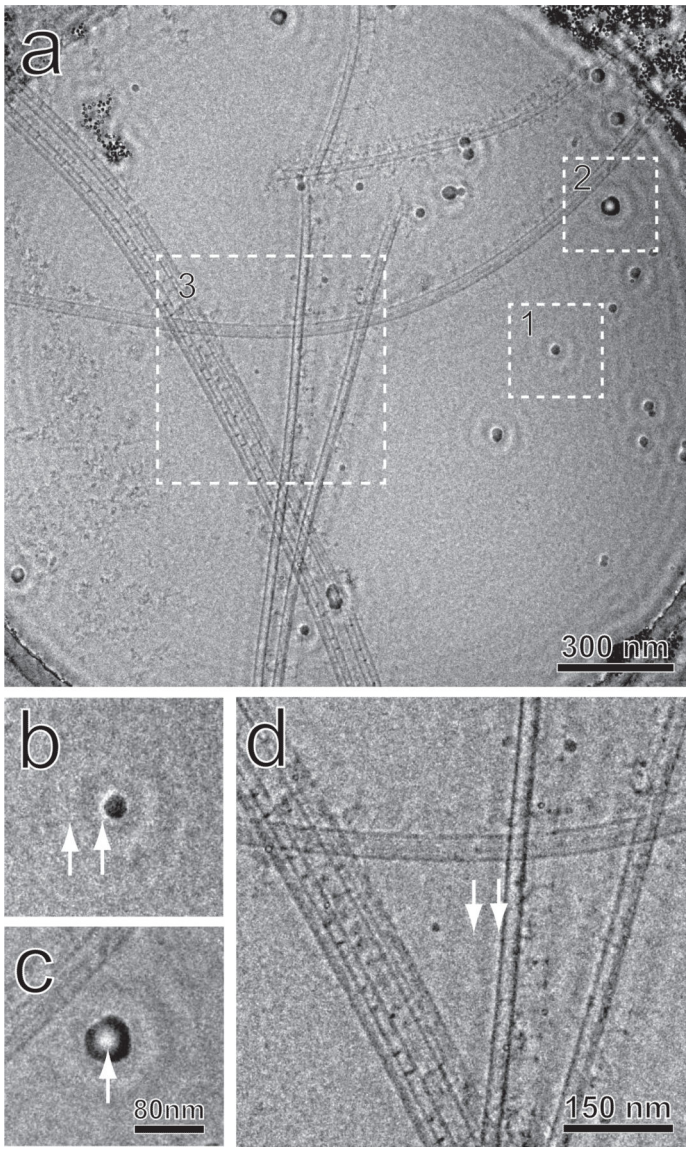

Fig. 1.

A zero-tilt micrograph from the tomographic series. (a) The entire field, (b) Region 1, a small contaminating ice particle used as a test object. (c) Region 2, a larger ice particle. (d) Region 3, a magnified view of the central area. Arrows in (b) and (d) indicate the halos and fringes caused by the cut-on of the Zernike phase plate. The arrow in (c) shows inverted contrast at the center of the particle.

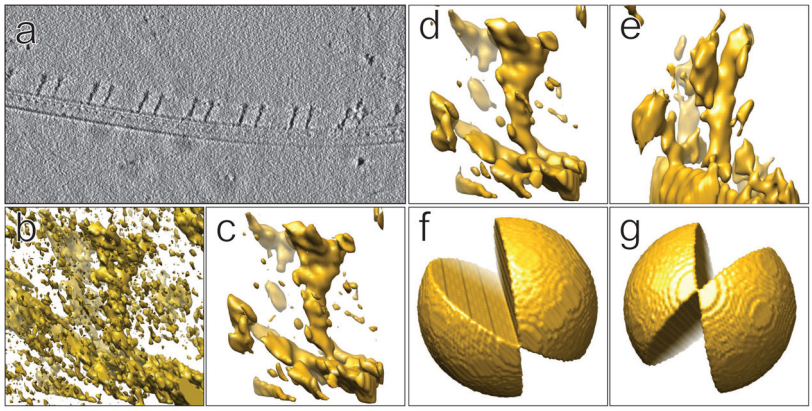

Fig. 2.

Structural maps of the radial-spoke complex. (a) A z-axis slice from the tomogram showing the array of radial spokes on a microtubule doublet. (b) A sub-volume extracted from the tomogram without any pre-reconstruction processing. (c) The same sub-volume as (b) after non-linear denoising by bilateral filtering. (d) The same sub-volume after low-frequency band-pass filtering, having an appearance very similar to (c). (e) A sub-volume with a missing wedge (as shown in Fig. 2g), from the same tomogram, after low-frequency band-pass filtering. (f) The Fourier missing-wedge corresponding to the sub-volume in Figs. 2b, 2c and 2d. (g) The missing wedge of the sub-volume in Fig. 2e

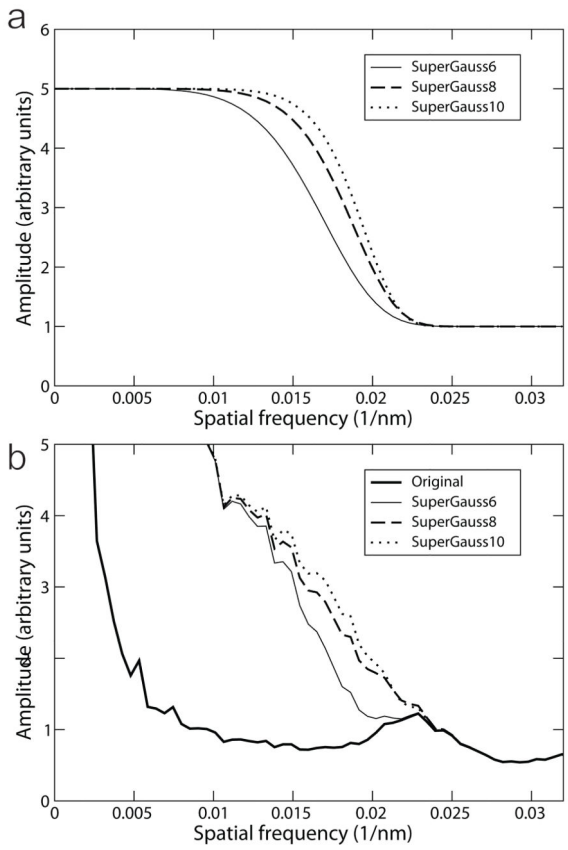

Fig. 3.

De-fringing by super-Gaussian functions. To carry out the de-fringing, super-Gaussian functions with various power values, shown in Fig. 3a, have been used to multiply the amplitudes of the original image, which is represented by the thick line in Fig. 3b. The resulting amplitude profiles are shown in (b), with thin, dashed and dotted lines representing the super-Gaussian of powers of 6, 8, and 10, respectively. The super-Gaussian filter with a power of 8 gave the smoothest amplitude profile.

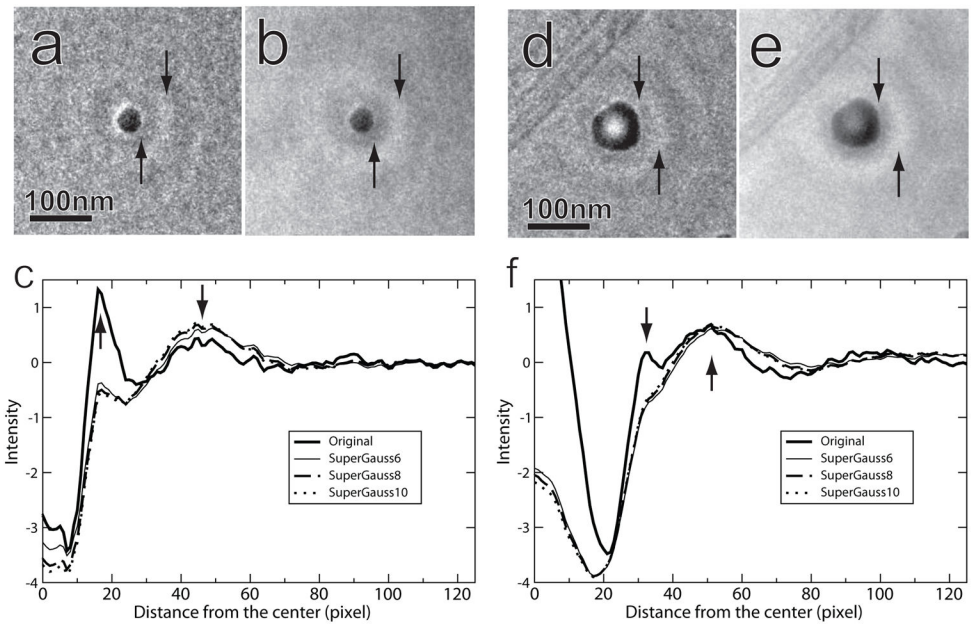

Fig. 4.

Results of de-fringing for objects of various sizes. The small (a) and large (d) particles were taken from Figs. 1b and 1c, respectively. (b) and (e) show the particles after de-fringing. The arrows in these images indicate the halo and the first bright fringe-ring. (c) and (f) display rotationally averaged intensity profiles, radially from the particle centers, demonstrating the effect of three different filter powers, compared to unfiltered images.

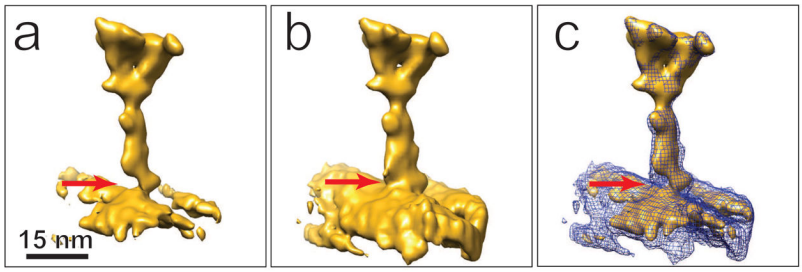

Fig. 5.

Structural map of the radial spoke complex obtained by sub-volume averaging from the ZPC tomogram, before (a) and after (b) the de-fringing correction. An artifactural density gap, indicated by the arrow, is present in the original map, and it is substantially corrected by de-fringing. The two maps are compared in (c), with the fringe-corrected map shown as a blue wire-frame model superimposed on the uncorrected model. Note that the head domains are almost identical, whereas the radial-spoke stalk and the microtubule are more filled-out in the de-fringed map.